Draft version December 30, 2019
Typeset using LaTeX default style in AASTeX62

Superflares on solar-type stars from the first year observation of *TESS*

Zuo-Lin Tu,[1] Ming Yang,[1,2] Z. J. Zhang,[1] and F. Y. Wang[1,2]

[1] *School of Astronomy and Space Science, Nanjing University, Nanjing 210093, China*
[2] *Key Laboratory of Modern Astronomy and Astrophysics (Nanjing University), Ministry of Education, Nanjing 210093, China*

ABSTRACT

Superflares, as strong explosions on stars, have been well studied with the progress of space time-domain astronomy. In this work, we present the study of superflares on solar-type stars using Transiting Exoplanet Survey Satellite (*TESS*) data. 13 sectors of observations during the first year of the *TESS* mission have covered the southern hemisphere of the sky, containing 25,734 solar-type stars. We verified 1,216 superflares on 400 solar-type stars through automatic search and visual inspection with 2-minute cadence data. Our result suggests a higher superflare frequency distribution than the result from *Kepler*. The reason may be that the majority of *TESS* solar-type stars in our dataset are rapidly rotating stars. The power-law index γ of the superflare frequency distribution ($dN/dE \propto E^{-\gamma}$) is constrained to be $\gamma = 2.16 \pm 0.10$, which is a little larger than that of solar flares but consistent with the results from *Kepler*. Because only 7 superflares of Sun-like stars are detected, we may not give a robust superflare occurrence frequency. And four stars are accompanied by unconfirmed hot planet candidates. Therefore, superflares are possibly caused by stellar magnetic activities instead of planet-star interactions. We also find an extraordinary star TIC43472154, which exhibits about 200 superflares per year. In addition, the correlation between energy and duration of superflares ($T_{\rm duration} \propto E^{\beta}$) is analyzed. We derive the power-law index to be $\beta = 0.42 \pm 0.01$, which is a little larger than $\beta = 1/3$ from the prediction according to magnetic reconnection theory.

Keywords: stars: flare - stars: solar-type

1. INTRODUCTION

Solar activities are closely connected with the lives of human beings. For example, solar winds can affect space weather, and trigger the geomagnetic storm on the Earth. Solar activities thus have great impacts on many fields, e.g. spacecraft electronics, commercial aviation, and radio communication (Choi et al. 2011). The Carrington event (Carrington 1859), which generated a very large solar flare with a total energy up to 10^{32} erg, caused widespread disruptions of telegraph systems and is considered to be one of the most severe solar storm. Indication of this event is also found in polar ice (Shea et al. 2006). However, the reliability of nitrate in ice records as a proxy for solar flares is strongly debated (Melott et al. 2016; Mekhaldi et al. 2017).

Solar flares are also studied by indirect methods, such as rapid increases of ^{14}C in tree rings. Four such events have been found (Miyake et al. 2012, 2013; Wang et al. 2017; Park et al. 2017). Basing on the quasi-simultaneous peaks of ^{10}Be and ^{36}Cl are found to associate with the peak of ^{14}C, solar superflares are considered as the physical origin (Mekhaldi et al. 2015; Miyake et al. 2019). However, the peaks of ^{10}Be and ^{36}Cl are adjusted to fit the ^{14}C peaks (Mekhaldi et al. 2015). So if the peaks are really simultaneous, solar origin is the most probable (Mekhaldi et al. 2015; Miyake et al. 2019). If these peaks are not correlated, other models may be possible (Neuhäuser & Hambaryan 2014, 2015; Wang et al. 2019).

Superflares are much stronger explosions than typical solar flares, with total energies varying from 10^{33} to 10^{38}erg and duration longer than an hour. The energy of a superflare is so high that can directly cause destructive attack to nearby living creatures. It therefore has attracted people's interests whether our Sun can generate superflares, just

Corresponding author: F. Y. Wang
fayinwang@nju.edu.cn

like the nine main sequence F8-G8 stars near our solar system (Schaefer et al. 2000). Previous studies have revealed a power-law relation between flare energy and frequency $dN/dE \propto E^{-\gamma}$ (Dennis 1985), which can be explained by self-organized criticality happening in a nonlinear energy dissipation system (e.g. Bak et al. 1987; Lu & Hamilton 1991; Aschwanden 2011; Wang & Dai 2013). For hard X-ray solar flares, γ is estimated to be 1.53 ± 0.02 by Crosby et al. (1993). For nano-flares and micro-flares, γ is 1.79 ± 0.08 (Aschwanden et al. 2000) and 1.74 (Shimizu 1995), respectively. With the help of *Kepler* space telescope, Maehara et al. (2012) detected 101 superflares on 24 slowly rotating solar-type stars and derived $\gamma = 2.0 \pm 0.2$, which is very similar to that of the distribution of solar flares. It therefore suggests the possibility of superflares occurring on the Sun, but with a comparatively lower frequency than rapidly rotating G-type stars.

There have been many observational and theoretical studies since the discovery of superflares on G-type stars with *Kepler* data. Shibayama et al. (2013) and Notsu et al. (2013) studied the connection between superflares and star spots by using more samples, and concluded that the energy of superflares is related to the star spot coverage, which is similar to the relation between solar flares and sunspots. Note that although the samples from Shibayama et al. (2013) were mistakenly mixed with some stars which are not in the main sequence, their conclusions are not changed (Notsu et al. 2019). Large star spots can be generated by solar dynamo mechanism (Shibata et al. 2013) and may store energy for superflares. Superflares, therefore, may share the same origin with solar flares. Because *Kepler* input catalog may not give accurate estimation of properties of solar-type stars, ground-based follow-up observations were also dedicated to the research, which has constrained stellar periodicity and spectrum information (Notsu et al. 2015a,b). Maehara et al. (2015) supported the comparability by extending the flares to lower energies using the 1-minute short-cadence data of *Kepler*. Karoff et al. (2016) also provided support by analyzing the chromospheric activities of 5,648 solar-like stars and 48 superflare stars in the field of view of both *Kepler* and Large Sky Area Multi-Object Fibre Spectroscopic Telescope (LAMOST).

On the other hand, there are different explanations on superflares. Rubenstein & Schaefer (2000) argued that a hot Jupiter companion can cause superflares on a solar-type star. Numerical simulations by Ip et al. (2004) also presented the importance of planet-star magnetic interactions on stellar activities. In addition, He et al. (2015) argued that the rotational modulation may be caused by faculae instead of star spots. And it is possible that flares and the magnetic features that dominate rotational modulation possibly have different source regions (He et al. 2018).

In this paper, we aim to detect superflares on solar-type stars using Transiting Exoplanet Survey Satellite (*TESS*) data. The primary goal of *TESS* is to find planets around bright nearby stars that enable further ground-based follow-up observations (Ricker et al. 2015). *TESS* has three advantages of studying stellar flares. Firstly, the stars observed by *TESS* are bright enough to achieve a high signal-to-noise ratio. Secondly, the 2-minute cadence allows the study of more detailed flare properties, such as duration and energy. Besides, to obtain more credible stellar parameters, the *TESS* input catalog (TIC) has imported data from other space and ground-based projects, such as *Gaia*-DR1&2 and LAMOST-DR1&DR3.

This paper is constructed as follows. In Section 2, we describe the methods to select solar-type stars and superflare candidates from the *TESS* data. Stellar periodicity and flare energy are also derived. The main results are described and discussed in Section 3, including the occurrence frequency of superflares, active flare stars, systems with exoplanets, and the correlation between duration and energy of superflares. Finally, we summarize our findings in Section 4.

2. DATA AND METHODS

2.1. *Selection of solar-type stars*

TESS was launched on April 18, 2018, and carried four identical cameras. During its first year of observations, *TESS* has scanned the southern hemisphere of the sky and obtained data products of 13 segments (sector 1 - sector 13). Each segment covers about 27 days. In this work, we adopt the Presearch Data Conditioned (PDC) light curves to avoid the instrumental systematics.

Firstly, the selection criteria of solar-type stars and Sun-like stars should be clarified. Solar-type stars are selected according to following criteria: (1) the surface effective temperature satisfies $5100\mathrm{K} \leqslant T_{\mathrm{eff}} < 6000\mathrm{K}$ and (2) the surface gravity in log scale $\log g > 4.0$ (Schaefer et al. 2000; Maehara et al. 2012). Besides, those solar-type stars with $5600\mathrm{K} \leqslant T_{\mathrm{eff}} < 6000\mathrm{K}$ and stellar periodicity > 10 days are considered as Sun-like stars. Totally, 26,034 targets meet the requirements based on the latest *TESS* input catalog v8 (TICv8, Stassun et al. 2019), which is expected to be the last version of TIC. Then, we examine these solar-type stars with the *Hipparcos*-2 catalog (van Leeuwen 2007) to exclude some confirmed binary stars. Totally, 145 stars are excluded from the dataset.

In contrast to *Kepler*, of which the pixel scale is about 4 arcsec, *TESS* has a larger pixel scale of 21 arcsec. 90% energy are ensquared by 4×4 pixels, namely encircled by radius of 42 arcsec (Ricker et al. 2015). So, it is possible that in one pixel of *TESS*, the primary object is contaminated by other stars. Therefore, we use *Gaia*-DR2 (Gaia Collaboration et al. 2018) to search stars within 42-arcsec radius nearby the primary solar-type star. Within 21 arcsec radius, we find 155 stars containing other brighter stars, which are excluded from the dataset. The reasons are: (1) flux from these brighter stars may significantly affect the light curves of main target; (2) in just one pixel scale (21 arcsec), we can not separate these brighter stars apart from main targets. Next, 2,849 solar-type stars, of which the nearby stars show surface effective temperature within 3000K-4000K, are flagged as possessing M-dwarf candidates. The reason why they are not excluded from the dataset is shown in Appdendix A.

2.2. *Selection of superflares*

The PDC light curves of the solar-type stars are used to search superflares. There have been several selection methods in literature. For example, clean light curves with only flare candidates can be acquired by fitting the quiescent variability (e.g. Walkowicz et al. 2011; Wu et al. 2015; Yang & Liu 2019). In addition, flare candidates can also be obtained by calculating the distribution of brightness changes between consecutive data points (e.g. Maehara et al. 2012; Shibayama et al. 2013; Maehara et al. 2015). In this paper, we choose the latter to detect superflares. According to Maehara et al. (2015), brightness changes between two pairs of consecutive points ΔF^2 is defined as :

$$\Delta F^2\left(t_{i,n}\right) = s\left(F_i - F_{i-n-1}\right)\left(F_{i+1} - F_{i-n}\right), \tag{1}$$

where F_i and t_i represent the flux and the time of the i-th data point, n is an integer number, and $s = \pm 1$. $s = 1$ when both $(F_i - F_{i-n-1}) > 0$ and $(F_{i+1} - F_{i-n}) > 0$, otherwise $s = -1$. ΔF^2 during a superflare event will become much larger than the quiescent situation. We set $n = 2$ to detect flare candidates with rise times larger than 4 minutes (Maehara et al. 2015). Besides, we also set $n = 5$ and obtained another group of ΔF^2 in case of missing flares with longer rise times. A data point is recognized as a flare candidate when its ΔF^2 is larger than the value at the top 1% of the ΔF^2 distribution by at least 3 times. We then located the peak data point for each flare candidate. To obtain a complete flare event, we use the data from 0.05 to 0.01 days before the peak and from 0.05 to 0.10 days after the peak in the case of $n = 2$, and use the data from 0.15 to 0.03 days before the peak and from 0.15 to 0.25 days after the peak in the case of $n = 5$. A quadratic function, $F_q(t)$, is adopted to remove the long-term stellar variability. The start time and end time of each flare candidate are the first and last point when $F(t) - F_q(t)$ is three times larger than the photometric error. We only reserve a flare candidate when (1) there are at least 3 consecutive points during the spike event, and (2) the decay time is longer than the rise time.

Then, we check each flare candidate by using pixel-level data to exclude false positives such as eclipses, random flux jumps, and cosmic rays. Firstly, we remove the candidates occurring simultaneously on different stars. Secondly, the pixel-level light curves during the flare event should match the optimal aperture given by *TESS*. Thirdly, visual inspection is applied to ensure the flare-like shape and obvious flux increases in pixel-level light curves as suggested by Wu et al. (2015). We present the example of a true flare event in Figure 1. The light curve of TIC121011020 in sector 4 perfectly shows a standard case of flare-shaped curve, with rapid rise and slow decay. Figure 2 shows a case with pixel-level fluctuations under the noise level. We exclude it from superflares since it is more likely to be a very weak flare or just noises. After excluding all the false positives, we finally find 1,216 superflares occurring on 400 solar-type stars.

2.3. *Periodicity estimation*

Periodicity of the solar-type stars are estimated through the Lomb-Scargle method (Lomb 1976; Scargle 1982), which is suitable for unevenly sampled data (VanderPlas 2018). We set the false alarm probability (FAP) to 10^{-4} to search the stellar period (e.g. Cui et al. 2019).

Figure 3 and Table 3 present the period distributions of the solar-type stars, superflares and flare stars. Note that we may miss some slowly rotating solar-type stars with $P > 10$ days because of the limited observing span. Most of the *TESS* targets were observed only in one sector, i.e. about 27 days, as shown in Figure 4. Therefore, periods longer than ∼14 days are not reliable for these targets. Totally, we obtain stellar periods for 3,827 slowly rotating ($P > 10$ days) solar-type stars and 22,207 fast rotating ($P < 10$ days) solar-type stars.

2.4. *Energy of superflares*

Following the method of Wu et al. (2015), the stellar luminosity can be estimated with the Stefan-Boltzmann law

$$L_* = 4\pi R_*^2 \sigma_{\rm sb} T_*^4, \tag{2}$$

where R_* and T_* are stellar radius and effective temperature given by TICv8, and $\sigma_{\rm sb}$ is the Stefan-Boltzmann constant. The flare energy thus can be calculated by integrating the fluxes within the flare event

$$E_{\rm flare} = \int L_* F_{\rm flare}\,(t) dt, \tag{3}$$

where $F_{\rm flare}\,(t)$ is the normalized flux above the fitted quadratic function (see section 2.2)

$$F_{\rm flare}\,(t) = F(t) - F_{\rm q}(t). \tag{4}$$

3. RESULTS

In Table 1, we list all parameters of 400 flare stars. Table 2 gives the parameters of 1216 superflares.

3.1. *Occurrence frequency distribution*

The observation mode of *TESS*, unlike *Kepler*, causes various observing spans for different targets. It is not suitable to calculate the occurrence frequency of superflare directly using the unequal observing spans. We therefore improve the method suggested by Maehara et al. (2012). First of all, we subdivided all the solar-type stars into different sets based on how many sectors the star was observed in. For example, Set-1 means that the stars were observed in only one sector. Similarly, Set-13 covers the stars observed in all the 13 sectors. The count of the solar-type stars in each Set-n can be found in Figure 4 and Table 4.

For each Set-n, the superflare frequency distribution as a function of flare energy is defined as

$$f_n = \frac{N_{\rm flares}}{N_{\rm stars} \cdot \tau_n \cdot \Delta E_{\rm flare}}, \tag{5}$$

where $N_{\rm flares}$ and $N_{\rm stars}$ are the numbers of superflares and solar-type stars in Set-n. $\Delta E_{\rm flare}$ represents the bin width of flare energy. τ_n can be calculated as

$$\tau_n = n \times 23.4 \text{ days}. \tag{6}$$

As the observing time is affected by satellite orbit, *TESS* may not observe fully and effectively for 27 days in each sector. Here, we calculated the mean value of continues observation length of each sector, which is 23.4 days. The final occurrence frequency of superflares for all the solar-type stars can be calculated as

$$f = \frac{\sum f_n}{13}. \tag{7}$$

Panel (a) of Figure 5 illustrates the distribution of flare peak amplitudes, i.e. the peak flux of $F_{\rm flare}(t)$ in Equation (4). Panel (b) presents the frequency distributions as a function of flare energy for all the solar-type stars (solid line), and slowly (dashed line) or rapidly (dotted line) rotating solar-type stars. After comparing the dotted line and dashed line, it is evident that rapidly rotating stars are much active than slowly rotating stars. According to the relation between stellar periodicity and age (Skumanich 1972; Barnes 2003), this result therefore indicates that younger solar-type stars generate superflares more frequently.

A power-law model is used to fit the frequency distributions

$$\frac{dN}{dE} \propto E^{-\gamma}. \tag{8}$$

The power-law index γ is fitted by using the same linear regression method of Tu & Wang (2018). For all solar-type stars, γ is 2.16 ± 0.10, which is consistent with $\gamma \sim 2.2$ from Shibayama et al. (2013) within 1σ interval, but higher than $\gamma \sim 1.5$ from Maehara et al. (2015). From panel (c) of Figure 5, it is obvious that hotter stars (with $5600\text{K} \leqslant T_{\rm eff} < 6000\text{K}$) have lower frequency than cooler stars (with $5100\text{K} \leqslant T_{\rm eff} < 5600\text{K}$). Above results are basically similar to those found from *Kepler* data (Maehara et al. 2012; Shibayama et al. 2013; Maehara et al. 2015).

Panel (d) compares the flare frequency derived by this work and by Maehara et al. (2015), which used the 1-minute short-cadence data of *Kepler* and therefore detected more flares in the low-energy region ($< 2 \times 10^{34}$ erg). In the

high-energy region ($> 2 \times 10^{34}$ erg), our superflare frequencies are higher than theirs. We speculate that this result is caused by the higher proportion of young stars in our dataset, as we have discussed above about panel (b). Since young stars rotate more rapidly and are more active, they can be more likely to generate superflares. Totally, 25,734 solar-type stars are selected, among which 21,955 stars have periods less than 10 days. The proportion of young stars is 85% in our work, compared to 32% in the work of Maehara et al. (2015). One may refer to Appendix B for more discussions about the potential changes caused by the number fraction of rapidly and slowly rotating stars.

The superflare frequency of Sun-like stars (dotted line) is also presented in panel (d) of Figure 5. For Sun-like stars (with 5100K $\leqslant T_{\rm eff} <$ 6000K and $P >$ 10 days), we obtain a higher frequency of superflares ($> 10^{35}$erg) than that from *Kepler* (Maehara et al. 2012; Shibayama et al. 2013; Maehara et al. 2015). However, there are only 7 such events, which are insufficient to robustly make a statistical conclusion. We look forward to more observations from *TESS* to extend the sample of Sun-like stars.

3.2. *Stellar period versus superflare energy*

An apparent negative correlation between flare frequency and stellar period have been found (Maehara et al. 2012; Notsu et al. 2013; Maehara et al. 2015). In Figure 6(b), in the range of stellar period over a few days, it is clear that the flare frequency decreases with the increase of rotation period. Similar result is found by Notsu et al. (2013) and Notsu et al. (2019). Moreover, stellar age has positive correlation with stellar period (Skumanich 1972; Barnes 2003). The result indicates that rapidly rotating stars, or young stars are more likely to generate superflares.

Notsu et al. (2019) found that the upper limit of flare energy in each period bin has a continuous decreasing trend with rotation period. From Figure 6(a), compared with the previous result (Figure 12(b) of Notsu et al. 2019), this trend is not obvious for the whole range of period. However, superflares within the period range over a few days (the tail part) clearly show the decreasing trend. We separate superflares into two parts according to their surface effective temperatures, which are shown in Figure 6 (c) and (d) respectively. Superflares with temperature 5600K $\leqslant T_{\rm eff} <$ 6000K perhaps show a little bit clearer decreasing trend for the whole period range, compared with panel (a). Similar decreasing trend can also be found in these two panels with period range over a few days (the tail part). As period is the key factor, we look forward to other methods precisely determining the periods of these solar-type stars (Appendix B). Meanwhile, slow-rotation stars ($P \sim 25$ days) are required to search specially, in order to statistically and strongly confirm this trend.

3.3. *Active flare stars*

Given that solar-type stars are grouped in different Set-n because of unequal observing spans, the flare frequency for an individual star is described by

$$f_* = \frac{N_{*\rm flares}}{\tau_*}, \tag{9}$$

where τ_* is continuous observation length of each flare star, and $N_{*\rm flares}$ denotes the number of flares from an individual star.

Table 5 and Table 6 list the top 20 stars sorted by flare frequency f_* and the number of flares $N_{*\rm flares}$, respectively. TIC43472154 is the most active star with an impressive flare frequency. If it is not coincidentally observed at an extraordinary active period, TIC43472154 can generate 233.17 flares per year. Besides, this star is not accompanied by any fainter stars or M dwarfs, according to the cross-match results from *Gaia* and *Hipparcos* data. This occurrence rate is much higher than that of KIC10422252, which is 41.6 flares per year (Shibayama et al. 2013). Figure 7 plots the light curve of TIC43472154. Superflares are marked with downward arrows.

Another target, TIC364588501, was observed by all sectors of *TESS* and exhibits the largest number of flares (63 flares). Additionally, like TIC43472154, this star is also a single star, according to the cross-match results from *Gaia* and *Hipparcos* data. TIC364588501 became more active than usual in the last 15 days of sector 5, and generated 15 superflares (Figure 8).

The most energetic superflare comes from TIC93277807, releasing 1.77×10^{37}erg in around 1.5 hr. This value consists with the inference that energy releasing through stellar flare is saturated at $\sim 2 \times 10^{37}$erg (Wu et al. 2015).

3.4. *Planet of flare stars*

Hot Jupiters are considered as one of the essential factors that can produce superflares on host stars (e.g. Rubenstein & Schaefer 2000; Ip et al. 2004). According to their studies, it is not possible for the Sun to generate superflares.

However, a lot of statistical works based on *Kepler* data did not detected hot Jupiters around flare stars (Maehara et al. 2012; Shibayama et al. 2013; Maehara et al. 2015).

We made a cross-check between our 400 flare stars with the Exoplanet Follow-up Observing Program for *TESS* (ExoFOP-*TESS*[1]). Cross matching results are listed in Table 7. There are four stars (TIC25078924, 44797824, 257605131, and 373844472) that have planet candidates. These four stars are unlikely to affect our statistical results. We thus did not exclude them in the analysis. Besides, there is only one star (TIC410214986) that possesses a confirmed hot planet (Newton et al. 2019). This is an interesting planet, and we list its parameters in Table 7, even if its hosting star (TIC410214986) is flagged as a binary system from the *Hipparcos*-2 catalog.

Compared with other stars, there is nothing special on the superflares of these four targets. Therefore, our results suggest that the planet-star interaction is unlikely to be a general mechanism for producing superflares.

Impacts of stellar activities towards their hosted planets have been studied comprehensively (e.g. Segura et al. 2010; Airapetian et al. 2016; Atri 2017; Lingam & Loeb 2017). Some reviews have briefly introduced what superflares would affect their hosted planets (e.g. Riley et al. 2018; Linsky 2019; Airapetian et al. 2019). Planets around flare stars may not only help us to understand planet-star interaction in generating flares, but also importantly extend our knowledge about how superflares will affect space weather of related planets. This will definitely improve our understanding about the relation between the Sun and the Earth as well. Much more space and ground-based missions will target on searching habitable planets. However their habitability is just simply decided by habitable zones. From a more foresighted aspect, it is also important and necessary to detailedly estimate habitability from impacts of their hosting stars' activities.

3.5. *Correlation between superflare energy and duration*

Maehara et al. (2015) proposed that the energy and duration of superflares are connected through power-law function, which was also proved by Tu & Wang (2018) using the statistical testing method. By applying magnetic reconnection theory, which has been widely accepted as the mechanism of solar flares, the correlation between the energy (E) and duration ($T_{\rm duration}$) of superflares can be denoted as

$$T_{\rm duration} \propto E^{1/3}. \tag{10}$$

Benefit from the 1-minute short-cadence data of *Kepler*, their duration and energy of superflares are estimated more accurate than using long-cadence data. The value of β is found to be 0.39 ± 0.03 (Maehara et al. 2015).

The 2-minute cadence of *TESS* also makes it possible to acquire accurate duration and energy of flares. We use the superflares detected in this paper and obtain $\beta = 0.42 \pm 0.01$, which is a little larger than the result from *Kepler*. Figure 9 presents the strong correlation between the duration and energy of superflares is our dataset.

Maehara et al. (2015) concluded that same physical mechanism may be shared by both solar flares and superflares of solar-type stars, according to their similarity. Later, Namekata et al. (2017) used solar white-light flares, and got $\beta = 0.38 \pm 0.06$, which is remarkably consistent with the result $\beta = 0.39 \pm 0.03$ of Maehara et al. (2015). This similarity may support that stellar superflares and solar flares are both generated by magnetic reconnections. But stellar superflares and solar white-light flares can not fitted by just one single power-law function, which indicates their potential difference. However, by using data of *Galaxy Evolution Explorer* (GALEX) missions, Brasseur et al. (2019) found that short-duration and near-ultraviolet flares do not show a strong correlation between energy and duration. Here, the observational values of β derived from *Kepler* and *TESS* are both larger than the theoretical prediction $\beta = 1/3$. Since this value is totally derived by the theory, which is successfully applied to solar flares. It may not precisely illustrate superflares on solar-type stars.

We consider magnetic field strength of Alfvén velocity ($v_A = B/\sqrt{4\pi\rho}$) as a variable, and assume that the pre-flare coronal density as a constant. The scaling power-law relation of equation (10) can be expressed as

$$T_{\rm duration} \propto E^{1/3} B^{-5/3}, \tag{11}$$

$$T_{\rm duration} \propto E^{-1/2} L^{5/2}, \tag{12}$$

where B is magnetic field strength and L is flaring length scale. For more detail introduction of this two relations, one may refer to Namekata et al. (2017). Using the coefficients obtained by Namekata et al. (2017), we also plot these two

[1] https://exofop.ipac.caltech.edu/tess/

scaling laws in Figure 9(b). Meanwhile, Solar white-light flares (Namekata et al. 2017) and superflares of solar-type stars found by using *Kepler* short-cadence data (Maehara et al. 2015) are also presented in the figure.

From this figure, the majority of superflares found in this work (blue circles) are with magnetic strength around 60G to 200G and length scales near 10^{10}cm to 10^{11}cm. Magnetic strength of superflares in this work are lower than that of superflares found by using *Kepler* short-cadence data (red squares). As we discuss in Section 2 and Appendix A, our method of selecting superflares basing on pixel-level data and bandpass of *TESS* tends to exclude weak flares with faint flare signal, which causes that the superflares of this work are with higher energy comparing with those of *Kepler* (from Figure 10(c)). Apparently, superflares have higher magnetic strength and larger flaring length than that of solar white-light flares. Superflares with lower energies tend to be generated from magnetic fields with higher strength and smaller flaring length scale. Contrarily, those superflares with higher energies tend to be from the weaker magnetic fields, and larger flaring length scales. In future, the observation of stellar magnetic strength and improvement of photometric imaging for precisely measuring flaring length scale will definitely advance our understanding of superflares. Also, as including more parameters of superflares in consideration, a closing-to-reality physical pattern will describe superflares in detail.

4. SUMMARY

In this work, 25,734 solar-type stars are selected from the first year's observations of *TESS* in the southern hemisphere of the sky. For the first time, we detect 1,216 superflares from 400 flare stars by using 2-minutes cadence data of *TESS*.

Statistical researches of these superflares are applied. We calculate the occurrence frequency distribution as a function of superflare energy. The power-law index γ of the superflare frequency distribution ($dN/dE \propto E^{-\gamma}$) is constrained to be $\gamma = 2.16 \pm 0.10$, which is consistent with the results from *Kepler*.

According to statistics from all solar-type stars, hotter stars (with 5600K $\leqslant T_{\rm eff} <$ 6000K) have lower superflare frequency than cooler stars (with 5100K $\leqslant T_{\rm eff} <$ 5600K). Besides, rapidly rotating stars (with $P <$ 10 days) are more active than slowly rotating stars (with $P >$ 10 days). These two conclusions are basically consistent with that of *Kepler* data.

It is worth mentioning that the frequency distributions calculated by using *TESS* data are overall higher than that from the *Kepler* data. The reason is that the majority of the solar-type stars in our dataset are rapidly rotating stars with stellar periodicities shorter than 10 days. Moreover, as only 7 superflares are detected on Sun-like stars, we may not be able to give a convincing conclusion on the frequency of superflares for Sun-like stars.

Some solar-type stars are very interesting in our dataset. For example, TIC43472154 is the most active star and has an occurrence rate of 233.17 superflares per year. TIC364588501 exhibits 63 superflares during the first year of the *TESS* mission. Additionally, several stars may have planet candidates. TIC410214986 has been confirmed to possess a hot planet. But this star is flagged as binary system by *Hipparcos*. Finally, the correlation between the energy and duration of superflares is calculated. The power-law index from *TESS* ($\beta = 0.42 \pm 0.01$) and *Kepler* ($\beta = 0.39 \pm 0.03$) are both larger than the theoretical value ($\beta = 1/3$), which is derived from the magnetic reconnection theory of solar flares.

A dataset containing superflares of solar-type stars has been constructed using the first year's observations of *TESS* for the first time. As *TESS* stars are bright and near, which are convenient for ground observations. In the future, photometric and spectrometric observations should be introduced for further studies of superflares. On the one hand, it is important to exclude those binary stars. Meanwhile, evolved stars (e.g. red giants and sub giants) potentially included in this work should be removed with newly spectrometric measurements of their surface temperatures and radii. Other methods (see Appendix B) should be applied for periodic estimation of flare stars, because period is a key parameter. High-resolution photometric observation will definitely be helpful to obtain clean light curves without any contamination from other fainter stars. On the other hand, for superflares, spectrometric information will be useful in tracking the chromospheric activities (Karoff et al. 2016). With high-resolution photometric observations, it will be easier to determine whether superflares come from the primary star. The Zwicky Transient Facility (ZTF) will simultaneously observe the northern hemisphere with *TESS* (van Roestel et al. 2019). Comparing the 21-arcsec pixel scale of *TESS*, the resolution of ZTF is 1 arcsec per pixel. The telescope will make nightly g- and r-band observations, which will offset deficiency of *TESS* bandpass on 400nm to 600nm. It may observe some less energetic flares with high-resolution imaging. Now, *TESS* is targeting the northern celestial hemisphere, which makes it possible to use the whole-sky data for studying superflares, and enlarging the dataset of superflares of Sun-like stars.

ACKNOWLEDGEMENTS

We thank an anonymous referee for constructive suggestions. We would like to thank Z.G. Dai, Y.F. Huang, X.F. Wu, H. Yu, B.B. Zhang and G.Q. Zhang for helpful discussions. N. Liu gave us helpful suggestions in cross matching works with data from *Gaia*-DR2 and *Hipparcos*-2 catalog. We sincerely thank Mikulski Archive for Space Telescopes (MAST) and TESS community for applying convenient data portal and tools. This work is supported by the National Natural Science Foundation of China (grant U1831207,11803012).

APPENDIX

A. *TESS* VERSUS *KEPLER*

Here, we note our considerations according to instrument features of *TESS*. The pixel scale ($\sim$ 21 arcsec) of *TESS* is five times larger than that ($\sim$ 4 arcsec) of *Kepler*. Around the whole sky, *TESS* attempt to search for planets transiting bright and nearby stars, which make it convenient for the ground follow-up observation. So, the pixel scale of *TESS* may not need to be with high-resolution as *Kepler*. But the larger pixel scale may also contain other energetic activities which are not from the primary objects, or the star is actually a binary star.

We first exclude binary stars in our dataset by using *Hipparcos*-2 catalog (HIP2) (van Leeuwen 2007). One thing should be noticed is that when we cross match HIP2, only 3,113 stars in our dataset contain the Hipparcos identifier (HIP), the remaining solar-type stars still can not be fully treated as single solar-type stars. They should be further confirmed by follow-up observation. As 145 binary stars only cost 4.7% of 3,113 stars, even if we exclude all binary stars, the flare frequencies may not be significantly changed.

Then, we use *Gaia*-DR2 (Gaia Collaboration et al. 2018) to search other unrelated stars which locate in the 42 arcsec radius of the primary solar-type stars. We exclude 155 stars, of which brighter stars locate within 21 arcsec. In another words, in just one pixel scale their flux will indistinguishably contaminate the primary objects. We have searched some M dwarfs within 42 arcsec radius, and they are distributed around with 2,849 solar-type stars. We do not exclude them from the data set for the following reasons: (1) M dwarfs should have 3000K $< T_{\rm eff} <$ 4000K, and $\log g > 4.0$ (e.g. Yang et al. 2017). *Gaia*-DR2 only provides surface effective temperature, but the surface gravity $\log g$ is not included in the catalog. Therefore, the searched targets are just candidates of M dwarfs. (2) Flare frequencies of M dwarfs are much larger than those of solar-type stars (a.k.a G dwarfs). But their flare energy ranges from $\sim 10^{31}$ to 10^{36} erg (Yang et al. 2017), and 95% flares are with energies $10^{32.40\pm1.35}$ erg. This energy range is much smaller than superflares on solar-type stars. So, even if M dwarfs are in the same aperture, the possibility that their flares contaminate dataset of this work is much lower. We demonstrate this idea in Figure 10(a). In the figure, histograms of flare energy in log scale of flares on M dwarfs (Doyle et al. 2019) and superflares on solar-type stars (this work) are shown. Solid curves give the fitting results by normal distribution. Flares on M dwarfs of Doyle et al. (2019) are detected also by using *TESS* data. Apparently, according to energy distributions of these two kinds of flares, superflares on solar-type stars are two orders of magnitude higher than flares on M dwarfs.

The bandpass filters for *TESS* and *Kepler* are different, 600 to 1000nm for *TESS* (Ricker et al. 2015), while 420 to 900nm for *Kepler* (Van Cleve & Caldwell 2016). Comparing these two bandpass filters, *TESS* is more sensitive to longer wavelengths, which is designed to detect much more M dwarfs. White-light flares detected from other stars can be described by blackbody radiation with effective temperature in ranges about 9,000K to 10,000K (e.g. Hawley et al. 2003; Kowalski et al. 2010), of which the peak emission is considered to be blue. Therefore, Doyle et al. (2019) have argued that according to the bandpass of *TESS*, it did not detect less energetic flares on M dwarfs. This idea is proved in Figure 10(b). In the figure, flare energy distributions of M dwarfs are from Yang et al. (2017) (by using *Kepler* data) and Doyle et al. (2019)(by using *TESS* data), which are colored by red and green, respectively. It is obvious that the flares detected by *TESS* have relatively higher energies than those from *Kepler*.

Similarly, in Figure 10(c), we compare energy distributions of superflares on solar-type stars, which are detected by *Kepler* (colored in magenta) and *TESS* (colored in blue). Note that, superflares detected by *Kepler* (Shibayama et al. 2013) may not totally be generated on main-sequence G-type dwarfs. So, first of all, we cross match the dataset of Shibayama et al. (2013) with the another catalog, in which radii of *Kepler* stars are revised by using *Gaia*-DR2 (Berger et al. 2018). Then, 496 superflares from main-sequence dwarfs are left. From the figure, we find that the superflares from our dataset have relatively higher energies than those from *Kepler* data. Therefore, *TESS* is more likely to detect relatively energetic flares. Same indication can also be found in Figure 5, where superflares with energies lower than 10^{35}erg show low frequency. These results are mainly caused by incomplete detection of flares with low energies.

B. THE NUMBER FRACTIONS OF SOLAR-TYPE STARS IN EQUATION OF STELLAR PERIODS

One thing should be kept in mind that there are potential differences between the observed and real number fraction of slowly and rapidly rotating stars. Following Appendix B of Notsu et al. (2019), we use the empirical gyrochronology relation to simply estimate the number fraction of solar-type stars in equation of period. This empirical relation can be written as (e.g. Mamajek & Hillenbrand 2008)

$$N_{\rm star}\left(P_{\rm rot} \geqslant P_0\right) = \left[1 - \frac{t_{\rm gyro}\left(P_0\right)}{\tau_{\rm MS}}\right] N_{\rm all}, \tag{B1}$$

where $t_{\rm gyro}\left(P_0\right)$ represents the stellar gyrochronological age in equation of period, which can be estimated by Equation (12)-(14) of Mamajek & Hillenbrand (2008). The corresponding $B-V$ values of different effective temperatures are estimated by Equation (3) of Ballesteros (2012). $\tau_{\rm MS}$ is the main-sequence phase, and here we set it as a constant ($\sim$ 10 Gyr) for all observation fields of *TESS*. One can refer to Appendix B of Notsu et al. (2019) for more specific calculation details. Here, we just list our results in Table 8.

From the table, we may notice that the number fraction of solar-type stars with over 10-days period in our dataset is five to seven times less than the roughly estimated values, and five to six times less than the results of *Kepler* field. Even though the flare frequency of slowly rotation star in Figure 5(b) and flare frequency in equation of period in Figure 6(b) can be five to seven times smaller, the dependency to period may not be changed significantly, as these changes are less than one order of magnitude. While considering more solar-type stars with period over 10 days, the number of flares should also statistically increase. Therefore, changes are much smaller than it looks. From another aspect, results roughly estimated by empirical relations may not be reliable (e.g. Tu et al. 2015; van Saders et al. 2016). We set the main-sequence phase as a constant for all *TESS* fields, which is not scientifically strict.

In the future, the main-sequence phase can be studied precisely for the field of each camera in each sector of *TESS* observation. Although estimation of longer stellar periods is hard under the limitation of *TESS*, we hope other methods can be applied to precisely determine periodicity of *TESS* stars. For example, through the auto-correlation function (ACF) (e.g. McQuillan et al. 2014), long periods can be determined by measuring rotational velocity by stellar spectrum (e.g. Reiners & Basri 2008; Browning et al. 2010; Reiners et al. 2012; Jeffers et al. 2018). As *TESS* is targeting the northern hemisphere, those stars which were observed by *Kepler* and *TESS* can use period estimation from the light curves of *Kepler* or other *Kepler* periodic catalog (e.g. McQuillan et al. 2014).

REFERENCES

Airapetian, V. S., Glocer, A., Gronoff, G., et al. 2016, Nature Geoscience, 9, 452

Airapetian, V. S., Barnes, R., Cohen, O., et al. 2019, arXiv e-prints, arXiv:1905.05093

Aschwanden, M. J. 2011, Self-Organized Criticality in Astrophysics

Aschwanden, M. J., Tarbell, T. D., Nightingale, R. W., et al. 2000, ApJ, 535, 1047

Atri, D. 2017, MNRAS, 465, L34

Bak, P., Tang, C., & Wiesenfeld, K. 1987, PRL, 59, 381

Ballesteros, F. J. 2012, EPL (Europhysics Letters), 97, 34008

Barnes, S. A. 2003, ApJ, 586, 464

Berger, T. A., Huber, D., Gaidos, E., et al. 2018, ApJ, 866, 99

Browning, M. K., Basri, G., Marcy, G. W., et al. 2010, AJ, 139, 504

Brasseur, C. E., Osten, R. A., & Fleming, S. W. 2019, ApJ, 883, 88

Carrington, R. C. 1859, MNRAS, 20, 13

Choi, H.-S., Lee, J., Cho, K.-S., et al. 2011, Space Weather, 9, 06001

Crosby, N. B., Aschwanden, M. J., & Dennis, B. R. 1993, SoPh, 143, 275

Cui, K., Liu, J., Yang, S., et al. 2019, arXiv e-prints, arXiv:1909.00189

Dennis, B. R. 1985, SoPh, 100, 465

Doyle, L., Ramsay, G., Doyle, J. G., et al. 2019, MNRAS, 489, 437

Gaia Collaboration, Brown, A. G. A., Vallenari, A., et al. 2018, A&A, 616, A1

Hawley, S. L., Allred, J. C., Johns-Krull, C. M., et al. 2003, ApJ, 597, 535

He, H., Wang, H., & Yun, D. 2015, ApJS, 221, 18

He, H., Wang, H., Zhang, M., et al. 2018, ApJS, 236, 7

Jeffers, S. V., Schöfer, P., Lamert, A., et al. 2018, A&A, 614, A76

Ip, W.-H., Kopp, A., & Hu, J.-H. 2004, ApJL, 602, L53

Karoff, C., Knudsen, M. F., De Cat, P., et al. 2016, Nature Communications, 7, 11058
Kowalski, A. F., Hawley, S. L., Holtzman, J. A., et al. 2010, ApJL, 714, L98
Lingam, M., & Loeb, A. 2017, ApJ, 848, 41
Linsky, J. 2019, Lecture Notes in Physics, Berlin Springer Verlag
Lomb, N. R. 1976, Ap&SS, 39, 447
Lu, E. T., & Hamilton, R. J. 1991, ApJ, 380, L89
Maehara, H., Shibayama, T., Notsu, S., et al. 2012, Nature, 485, 478
Maehara, H., Shibayama, T., Notsu, Y., et al. 2015, Earth, Planets, and Space, 67, 59
Mamajek, E. E., & Hillenbrand, L. A. 2008, ApJ, 687, 1264
McQuillan, A., Mazeh, T., & Aigrain, S. 2014, ApJS, 211, 24
Mekhaldi, F., et al., 2015, Nature Communications, 6, 8611
Mekhaldi, F., et al., 2017, JGR Atmospheres, 122, 11900
Melott, A. L., et al., 2016, JGR Atmospheres, 121, 3017
Miyake, F., Nagaya, K., Masuda, K., et al. 2012, Nature, 486, 240
Miyake, F., Masuda, K., & Nakamura, T. 2013, Nature Communications, 4, 1748
Miyake, F., Usoskin, I., Poluianov, S., et al., 2019, Extreme Solar Particle Storms, IOP Publishing
Namekata, K., Sakaue, T., Watanabe, K., et al. 2017, ApJ, 851, 91
Neuhäuser, R., & Hambaryan, V. V. 2014, Astronomische Nachrichten, 335, 949
Neuhäuser, R., & Hambaryan, V. V. 2015, Astronomische Nachrichten, 336, 930
Newton, E. R., Mann, A. W., Tofflemire, B. M., et al. 2019, ApJL, 880, L17
Notsu, Y., Shibayama, T., Maehara, H., et al. 2013, ApJ, 771, 127
Notsu, Y., Honda, S., Maehara, H., et al. 2015a, PASJ, 67, 32
Notsu, Y., Honda, S., Maehara, H., et al. 2015b, PASJ, 67, 33
Notsu, Y., Maehara, H., Honda, S., et al. 2019, ApJ, 876, 58
Park, J. et al., 2017, Radiocarbon, 59, 1147
Reiners, A., & Basri, G. 2008, ApJ, 684, 1390
Reiners, A., Joshi, N., & Goldman, B. 2012, AJ, 143, 93
Ricker, G. R., Winn, J. N., Vanderspek, R., et al. 2015, Journal of Astronomical Telescopes, Instruments, and Systems, 1, 014003
Riley, P., Baker, D., Liu, Y. D., et al. 2018, SSRv, 214, 21
Rubenstein, E. P. & Schaefer, B. E. 2000, ApJ, 529, 1031
Scargle, J. D. 1982, ApJ, 263, 835
Schaefer, B. E., King, J. R., & Deliyannis, C. P. 2000, ApJ, 529, 1026
Segura, A., Walkowicz, L. M., Meadows, V., et al. 2010, Astrobiology, 10, 751
Shea, M. A., Smart, D. F., McCracken, K. G., et al. 2006, Advances in Space Research, 38, 232
Shibayama, T., Maehara, H., Notsu, S., et al. 2013, ApJS, 209, 5
Shibata, K., Isobe, H., Hillier, A., et al. 2013, PASJ, 65, 49
Shimizu, T. 1995, PASJ, 47, 251
Skumanich, A. 1972, ApJ, 171, 565
Stassun, K. G., Oelkers, R. J., Paegert, M., et al. 2019, AJ, 158, 138
Tu, L., Johnstone, C. P., Güdel, M., et al. 2015, A&A, 577, L3
Tu, Z. L., & Wang, F. Y. 2018, ApJL, 869, L23
VanderPlas, J. T. 2018, The Astrophysical Journal Supplement Series, 236, 16
Van Cleve, J. E., & Caldwell, D. A. 2016, Kepler Science Document
van Leeuwen, F. 2007, A&A, 474, 653
van Roestel, J., Bellm, E. C., Duev, D. A., et al. 2019, Research Notes of the American Astronomical Society, 3, 136
van Saders, J. L., Ceillier, T., Metcalfe, T. S., et al. 2016, Nature, 529, 181
Walkowicz, L. M., Basri, G., Batalha, N., et al. 2011, AJ, 141, 50
Wang, F. Y., & Dai, Z. G. 2013, Nature Physics, 9, 465
Wang, F. Y., Li, X. Y., Chernyshov, D. O., et al., 2019, arXiv:1911.03209
Wang, F. Y., Yu, H., Zou, Y. C., et al. 2017, Nature Communications, 8, 1487
Wu, C.-J., Ip, W.-H., & Huang, L.-C. 2015, ApJ, 798, 92
Yang, H., Liu, J., Gao, Q., et al. 2017, ApJ, 849, 36
Yang, H., & Liu, J. 2019, ApJS, 241, 29

Table 1. Flare stars

TESS ID	$T_{\rm eff}$ [a] (K)	$\log g$ [b]	Radius [c] ($R_\odot$)	Period [d] (days)	Flares [e]	Set-n [f]	f_* [g] (year^{-1})	Flag [h]
737327	5872	4.20	1.35	1.62	1	1	14.57	GM
1258935	5739	4.48	0.97	4.93	1	1	19.37	
6526912	5541	4.24	1.25	2.29	1	1	14.39	
7491381	5692	4.47	0.96	2.21	4	3	21.37	
7586485	5801	4.36	1.11	1.76	6	2	46.11	
11046349	5409	4.31	1.12	3.33	2	1	29.48	GM
12359032	5471	4.51	0.90	2.32	2	1	27.98	
12393800	5571	4.19	1.31	1.03	1	1	13.99	
13955147	5701	4.44	1.01	2.22	1	2	7.69	
15444490	5598	4.09	1.49	1.98	2	2	15.85	

NOTE.
[a] Effective surface temperature in unit of K.
[b] Surface gravity of star in log scale.
[c] Stellar radii in unit of solar radius $R_\odot$.
[d] Stellar periods in unit of days.
[e] Number of flares of each star (same as $N_{*\rm flares}$ of Equation (9)).
[f] Number of Set-n which defined in Section 3.1.
[g] Flare frequency deduced by Equation (9).
[f] Flags of flare stars, where GM means the star may possess M dwarfs candidates nearby (42 arcseconds from the main target). GB stand for there are stars, which are brighter than the main stars, and 21 to 42 arcseconds from the main targets. (A portion of data is shown here.The full data is available in machine-readable form online.)

Table 2. Superflares

TESS ID	Peak Date [a]	Peak Flux [b] (erg s^{-1})	Energy [c] (erg)	Duration [d] (s)
737327	1460.1798	5.02E+31	5.58E+34	1919.98
1258935	1517.6755	4.71E+31	3.97E+34	1560.03
6526912	1673.3840	3.78E+32	9.46E+35	5759.94
7491381	1469.0019	1.10E+32	7.96E+34	1559.99
7491381	1470.5130	4.08E+31	9.09E+34	3359.98
7491381	1486.3100	3.71E+31	2.32E+34	959.98
7491381	1489.2516	6.92E+31	2.12E+35	6959.85
7586485	1411.2694	5.53E+31	6.91E+34	2640.06
7586485	1428.4168	3.61E+31	4.75E+34	2520.01
7586485	1440.9098	2.07E+31	1.39E+34	959.99
7586485	1442.7237	9.31E+31	5.07E+34	1559.99
7586485	1447.3084	3.15E+31	4.37E+34	2279.97
7586485	1457.0429	3.82E+31	8.09E+34	3599.92

NOTE.
[a] The corresponding date of superflares' peak.
[b] Flux of peak calculated by $L_* F_{\rm flare}(t)$, when t equals to the peak time. L_* and $F_{\rm flare}(t)$ are defined in Equation 2 and Equation 4.
[c] Energy of superflare.
[d] Duration of superflare in unit of second.
(A portion of data is shown here.The full data is available in machine-readable form online.)

Table 3. Numbers of solar-type stars, superflares, flare stars of each periodic bins.

log P	Solar-type Stars	Superflares	Flare Stars
-1.00	585	2	2
-0.81	606	8	1
-0.62	408	22	9
-0.43	372	46	13
-0.24	390	95	28
-0.05	543	136	41
0.14	919	295	80
0.33	2900	317	90
0.52	4486	217	82
0.71	7410	50	35
0.90	5728	22	16
1.10	1151	2	2
1.29	113	4	1
1.48	111	0	0
1.67	7	0	0
1.86	3	0	0
2.05	2	0	0

NOTE.
$\log P$ represents stellar periodicity in log scale.

Table 4. Numbers of solar-type stars, superflares, flare stars of each Set-n.

Set-n	5100K $\leqslant T_{\rm eff} <$ 5600K						5600K $\leqslant T_{\rm eff} <$ 6000K						Total		
	$P <$ 10 days			$P >$ 10 days			$P <$ 10 days			$P >$ 10 days					
	$N_{\rm star}$	$N_{\rm flare}$	$N_{\rm fstar}$	$N_{\rm star}$	$N_{\rm flare}$	$N_{\rm fstar}$	$N_{\rm star}$	$N_{\rm flare}$	$N_{\rm fstar}$	$N_{\rm star}$	$N_{\rm flare}$	$N_{\rm fstar}$	$N_{\rm star}$	$N_{\rm flare}$	$N_{\rm fstar}$
1	7023	249	128	1204	0	0	8798	113	67	1018	5	2	18043	367	197
2	1465	233	67	406	0	0	1894	113	36	335	0	0	4100	346	103
3	326	34	14	88	0	0	471	39	14	80	1	1	965	74	29
4	92	16	3	24	0	0	123	11	3	14	0	0	253	27	6
5	73	0	0	19	0	0	109	0	0	15	0	0	216	0	0
6	54	18	2	14	0	0	68	18	3	21	0	0	157	36	5
7	39	65	5	16	0	0	63	3	1	13	0	0	131	68	6
8	37	1	1	15	0	0	48	5	2	15	0	0	115	6	3
9	80	31	5	29	0	0	90	1	1	25	0	0	224	32	6
10	62	25	2	35	0	0	73	3	2	28	0	0	198	28	4
11	91	20	6	44	4	1	115	10	3	35	0	0	285	34	10
12	182	29	5	77	1	1	213	23	8	59	1	1	531	54	15
13	173	38	5	76	0	0	193	106	11	74	0	0	516	144	16
Total	9697	759	243	2047	5	2	12258	445	151	1732	7	4	25734	1216	400

NOTE.
The definition of Set-n is in Section 3.1. Basically, according to stellar surface temperature and rotation period, we classify solar-type stars into four categories for each Set-n. $N_{\rm star}$, $N_{\rm flar}$, $N_{\rm fstar}$ represent the numbers of solar-type stars, flares and flare stars, respectively. The total numbers are also listed in the last three columns and the last row.

Table 5. Stellar properties of flare stars sorted by star activity f_*.

TESS ID	$T_{\rm eff}$ [a] (K)	$\log g$ [b]	Radius [c] ($R_\odot$)	Period [d] (days)	Flares [e]	Set-n [f]	f_* [g] (year^{-1})
43472154	5316	4.49	0.90	2.80	16	1	233.17
92845906	5634	4.17	1.37	2.07	22	2	175.12
53417036	5555	4.44	0.98	1.53	8	1	140.26
20096356	5458	4.46	0.95	0.79	16	2	127.34
175491080	5321	4.52	0.88	3.98	14	2	122.71
206592394	5597	4.54	0.88	3.43	8	1	111.91
38402758	5472	4.42	1.00	1.08	6	1	97.62
127311608	5515	4.23	1.25	0.96	5	1	93.24
382575967	5567	4.42	1.01	2.19	40	7	91.36
284789252	5789	4.41	1.05	0.87	6	1	88.45
92347098	5234	4.48	0.90	3.93	5	1	81.34
152346470	5844	4.14	1.44	1.97	5	1	81.08
78055898	5495	4.30	1.14	4.07	10	2	79.59
257644579	5916	4.38	1.11	1.51	10	2	76.86
364588501	5605	4.26	1.22	2.28	63	13	75.35
272456799	5874	4.14	1.46	2.18	4	1	74.60
21540586	5417	4.27	1.18	1.35	9	2	71.63
93277807	5706	4.17	1.37	3.89	4	1	70.15
32874669	5147	4.53	0.84	4.73	4	1	70.15
302116397	5531	4.39	1.05	0.95	5	1	67.93

NOTE.
Top 20 flare stars sorted by flare frequency (f_*). Headers of this table are the same as Table 1.

Table 6. Stellar properties of flare stars sorted by number of flares.

TESS ID	$T_{\rm eff}$ [a] (K)	$\log g$ [b]	Radius [c] ($R_\odot$)	Period [d] (days)	Flares [e]	Set-n [f]	f_* [g] (year^{-1})
364588501	5605	4.26	1.22	2.28	63	13	75.35
382575967	5567	4.42	1.01	2.19	40	7	91.36
149539114	5367	4.36	1.05	0.43	22	10	36.05
92845906	5634	4.17	1.37	2.07	22	2	175.12
260162387	5855	4.20	1.35	1.98	18	13	21.63
167163906	5465	4.55	0.86	0.76	18	12	23.44
279572957	5570	4.34	1.11	1.81	16	9	27.86
43472154	5316	4.49	0.90	2.80	16	1	233.17
20096356	5458	4.46	0.95	0.79	16	2	127.34
167574282	5291	4.53	0.86	1.70	14	13	16.73
175491080	5321	4.52	0.88	3.98	14	2	122.71
339668420	5395	4.47	0.93	4.84	12	6	32.34
219389540	5744	4.44	1.02	1.55	11	6	29.32
257644579	5916	4.38	1.11	1.51	10	2	76.86
78055898	5495	4.30	1.14	4.07	10	2	79.59
38827910	5304	4.53	0.86	3.66	10	11	14.14
348898049	5226	4.71	0.69	1.00	9	13	10.76
219212899	5217	4.55	0.83	4.06	9	7	20.53
21540586	5417	4.27	1.18	1.35	9	2	71.63
260268898	5186	4.58	0.80	2.25	8	9	13.97

NOTE.
Top 20 flare stars sorted by number of flares on the corresponding star. Headers of this table are the same as Table 5.

Table 7. Properties of flare stars hosting planets.

Host Star *TESS* ID	Planet ID	Period [a] (Days)	Radius [b] ($R_\oplus$)	Equilibrium Temp. [c] (K)	Information [d]
25078924	TIC25078924.01	0.9097	14.43	–	Community TESS Objects of Interest
25078924	TIC25078924.02	0.9035	28.70	–	Community TESS Objects of Interest
44797824	TOI865.03	0.7456 ± 0.000018	3.79 ± 2.57	752	TESS Object of Interest
257605131	TOI451.01	8.1855 ± 0.00177	3.95 ± 0.69	640	TESS Object of Interest
257605131	TIC257605131.02	1.8578	1.85 ± 0.06	1337	Community TESS Objects of Interest
257605131	TIC257605131.03	3.0643	1.82 ± 0.22	1132	Community TESS Objects of Interest
373844472	TOI275.01	0.9195 ± 0.000004	17.94 ± 18.68	1886	TESS Object of Interest
410214986*	DS Tuc A b	8.1383 ± 0.000011	5.70 ± 0.17	850	Confirmed Planets

NOTE.
Planetary properties which are cross matched with ExoFOP-*TESS*. Note that some values are not shown errors as their error values are not included in the ExoFOP-*TESS* catalog.
[a] Orbital period of planet.
[b] Radius of planet in unit of the earth radius $R_\oplus$.
[c] Equilibrium temperature, which represents theoretical estimated temperature of planets heated by their host star.
[d] Give information about each planet. Community TESS Objects of Interest (CTOIs) are planetary systems or potentially interesting targets identified by the community members, but not treated as a TESS Object of Interest (TOI) by the TESS project. TOI are preliminary TESS Objects of Interest, which are structured by The TESS Science Office (TSO) list, The Mikulski Archive for Space Telescopes (MAST) list and The Exoplanet Follow-up Observing Program for TESS (ExoFOP-TESS) list.
*Most of planets listed here are still not confirmed. DS Tuc A b is a hot planet, which is confirmed in ExoFOP-*TESS* list [a]. But the hosting star TIC410214986 is flaged as binary stars by *Hipparcos*.

[a]https://exoplanetarchive.ipac.caltech.edu/

Table 8. Number fractions of solar-type stars

Data set	5100K $\leqslant T_{\rm eff} <$ 5600K		5600K $\leqslant T_{\rm eff} <$ 6000K	
	$N_{\rm star}(P < 10\ {\rm days})/N_{\rm all}$	$N_{\rm star}(P \geqslant 10\ {\rm days})/N_{\rm all}$	$N_{\rm star}(P < 10\ {\rm days})/N_{\rm all}$	$N_{\rm star}(P \geqslant 10\ {\rm days})/N_{\rm all}$
Gyrochronology relation[a]	5.1% – 7.1%	92.9% – 94.9%	7.1% – 10.9%	89.1% – 92.9%
Notsu et al. (2019)[b]	14.1%	85.9%	21.7%	78.3%
This work	82.6%	17.4%	87.6%	12.4%

NOTE.
Here, we separate solar-type stars into two parts according to their surface effective temperatures. $N_{\rm star}(P < 10\ {\rm days})/N_{\rm all}$ denotes the number fraction between stars with period less than 10 days and all stars. (a) gives the results calculated by Equation B1. (b) lists the results shown in Table 9 of Notsu et al. (2019), who used the reported stellar periods in McQuillan et al. (2014).

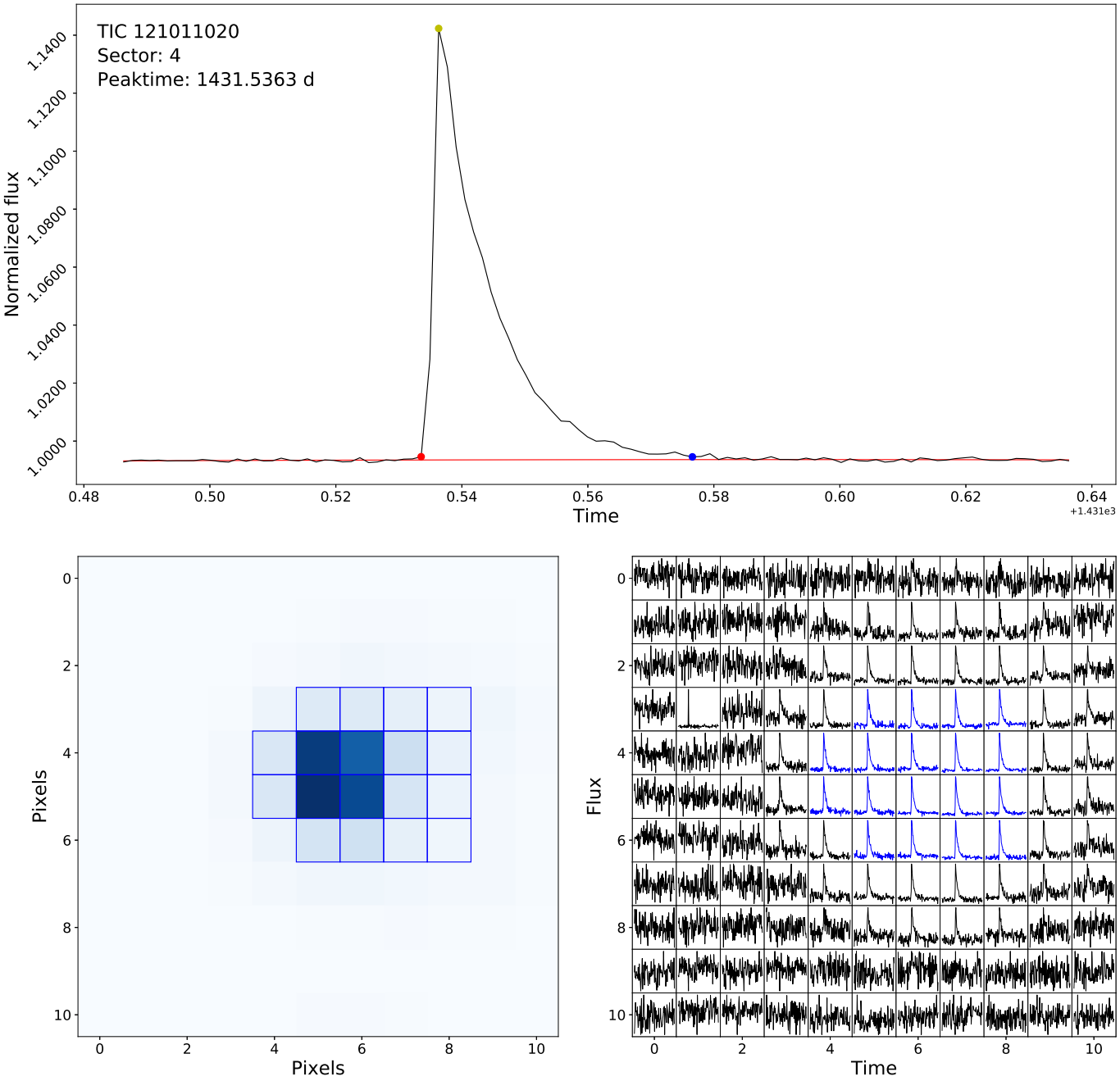

Figure 1. An example of a true flare event. The upper panel gives flare light curve of TIC121011020. Black solid line stands for normalized flux $F(t)$. Flux fitted by quadratic function ($F_{\rm q}(t)$) is shown as red solid line. The red, yellow and blue points represent begin, peak and end time of the flare, respectively. The light curve in this panel shows a standard flare shape with rapid rise and slow decay. The lower-left panel shows pixel level data at the peak time. The blue frames encircle *TESS* pipeline aperture masks. Those pixels are masked with deeper blue, of which flux are greater than others. In the lower-right panel, we present light curve of each target pixel, which corresponds to the every single block in lower-left penal. Blue light curves stand for *TESS* pipeline aperture masks. We may realize from this panel that, the flare-shape light curves are distributed as PSF.

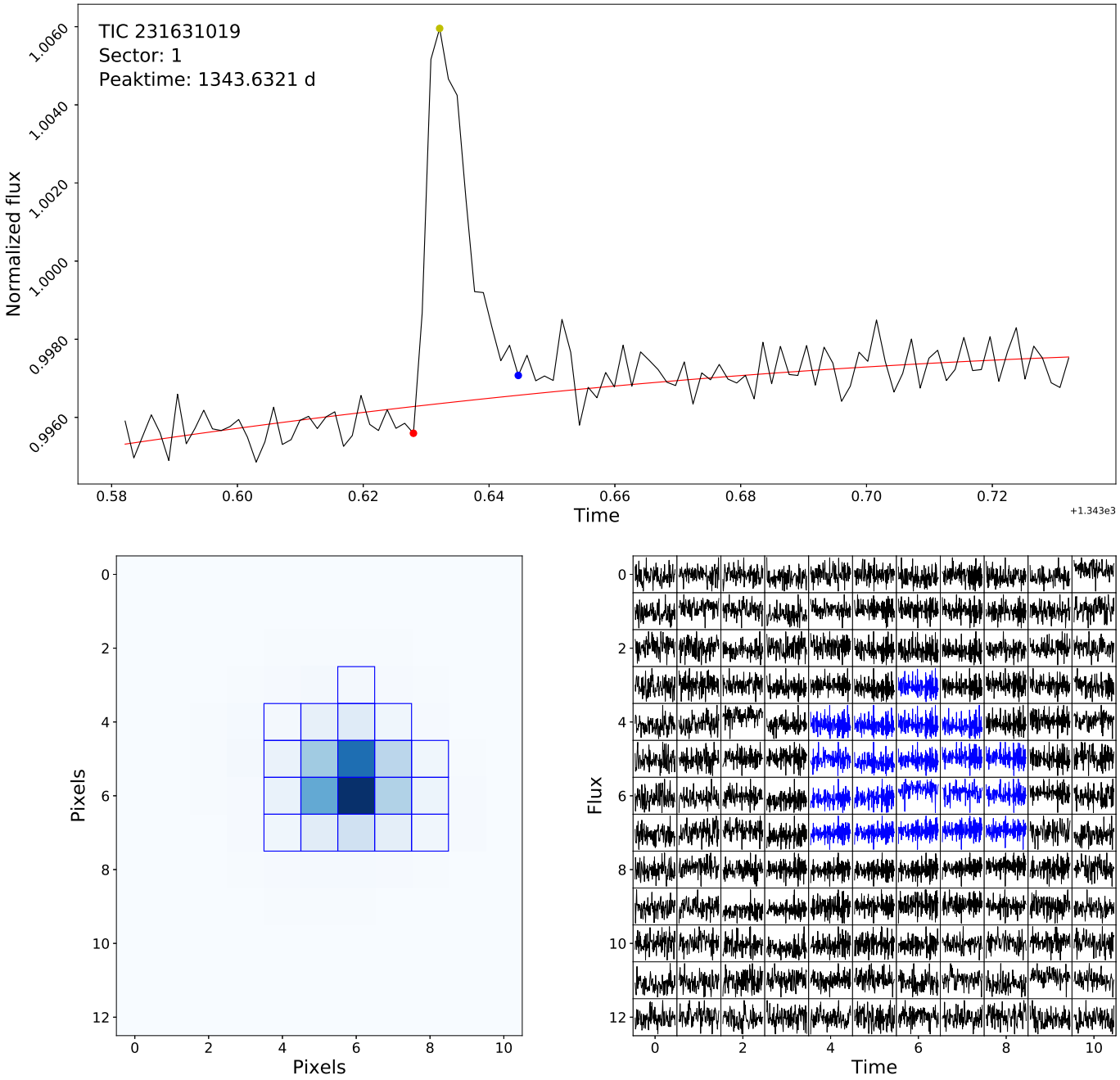

Figure 2. Same as Figure 1, but for a false event or a very weak flare, which is excluded from flare candidates. In the lower-right panel, unlike what we perceive from Figure 1, it may not show light curves distributed as PSF. But the noise level flux has been flooded in all pixels.

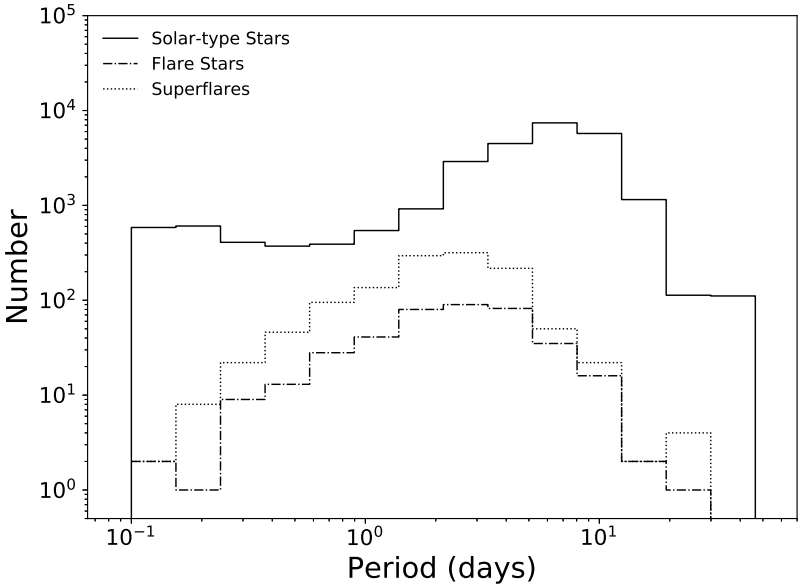

Figure 3. Periodic distribution of solar-type stars (solid line), superflares (dotted line), and flare stars (dashed line). Table 3 lists the corresponding values of each subset.

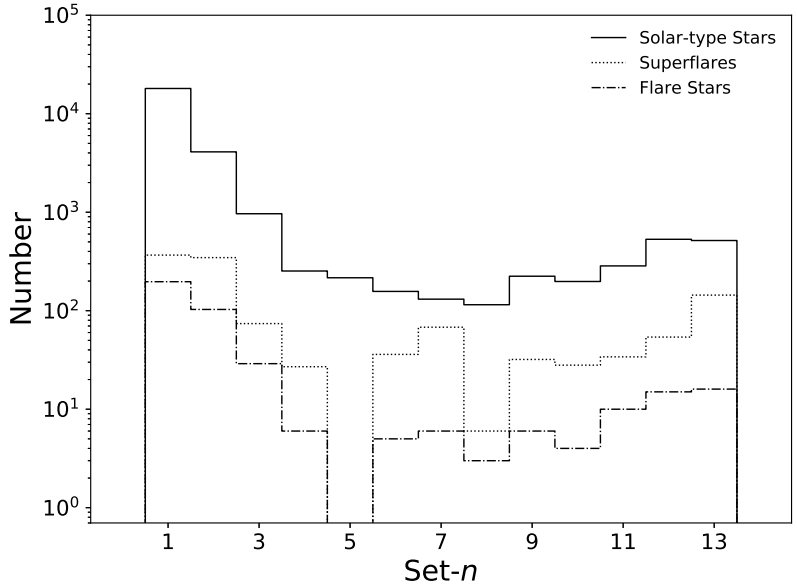

Figure 4. Distribution of solar-type stars (solid line), superflares (dotted line), and flare stars (dashed line) in each Set-n subset. The definition of Set-n can be found in Section 3.1. Table 4 lists the corresponding values of each subset.

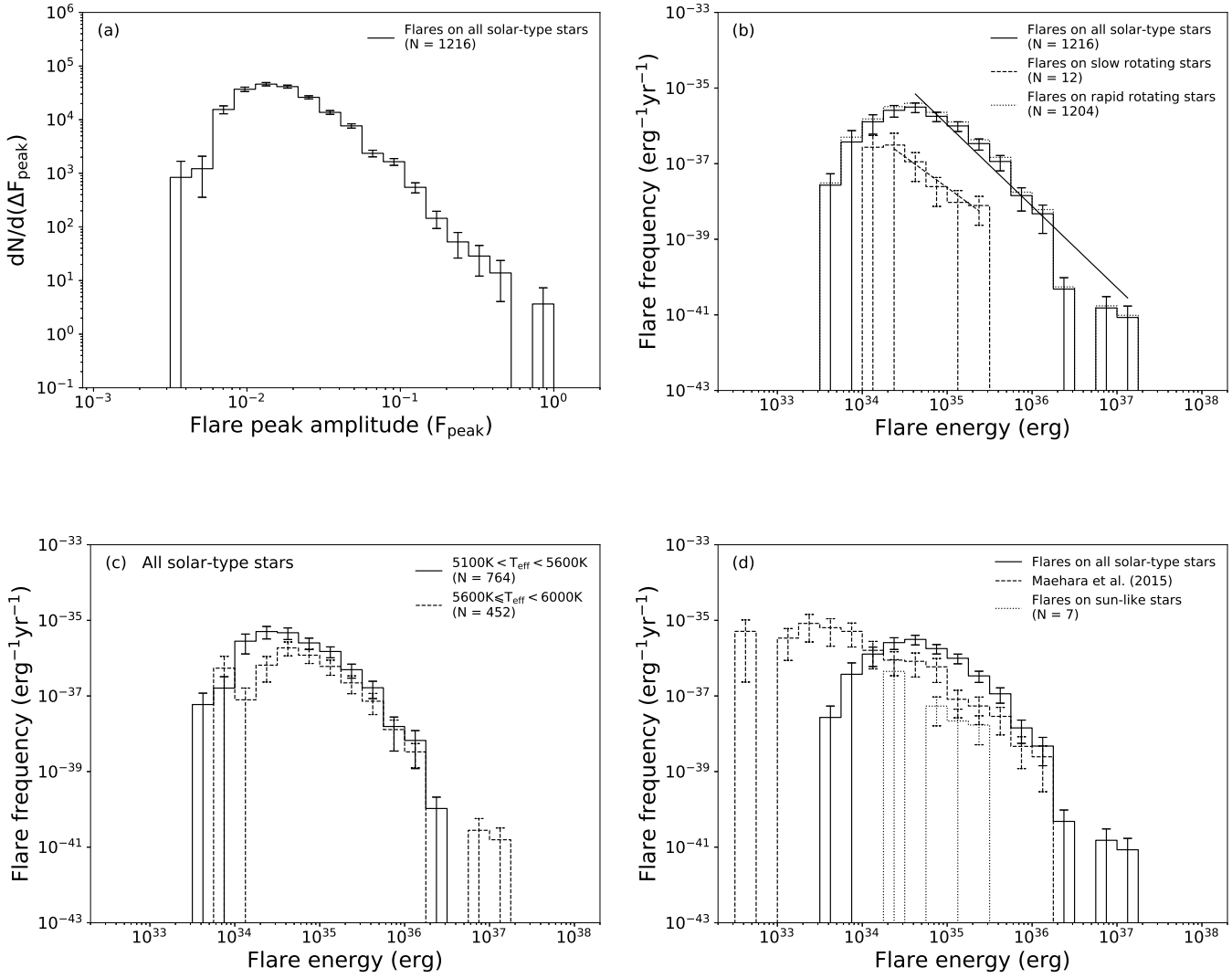

Figure 5. (a) Frequency distribution of normalized peak flux $F_{\rm peak} = F(t_{\rm peak}) - F_q(t_{\rm peak})$ at time $t_{\rm peak}$. All 1,216 superflares are included. (b) Frequency distribution of flare energy. Solid line represents all 1,216 solar-type stars (with 5100K $\leqslant T_{\rm eff} <$ 6000K and $\log g > 4.0$), and dashed line expresses 12 superflares of slowly rotating solar-type stars (with period $P > 10$ days). Two straight lines show the best-fit power-law distribution of $dN/dE \propto E^{-\gamma}$. Solid line gives $\gamma \sim 2.16 \pm 0.10$, and dashed line gives $\gamma \sim 1.64 \pm 0.44$. Doted line stands for 1204 flares on rapidly rotating stars, of which frequency distributions are almost overlap with solid line. (c) Same frequency distribution as panel (b) but for different effective surface temperatures. Solid and dashed lines represent dataset of 5100K $\leqslant T_{\rm eff} <$ 5600K and 5600K $\leqslant T_{\rm eff} <$ 6000K respectively. (d) Solid line indicates the same frequency distribution of solid line in panel (b). In contrast with the result of *Kepler* short-cadence data, we imported result from Figure 3(b) of Maehara et al. (2015) as dashed line. The dotted line indicates frequency distribution of Sun-like stars with effective temperature 5600K $\leqslant T_{\rm eff} <$ 6000K and period $P > 10$ days. However, only 7 flares satisfy the two criteria. In all panels, the error bars are given by the square root of flare numbers in each bins.

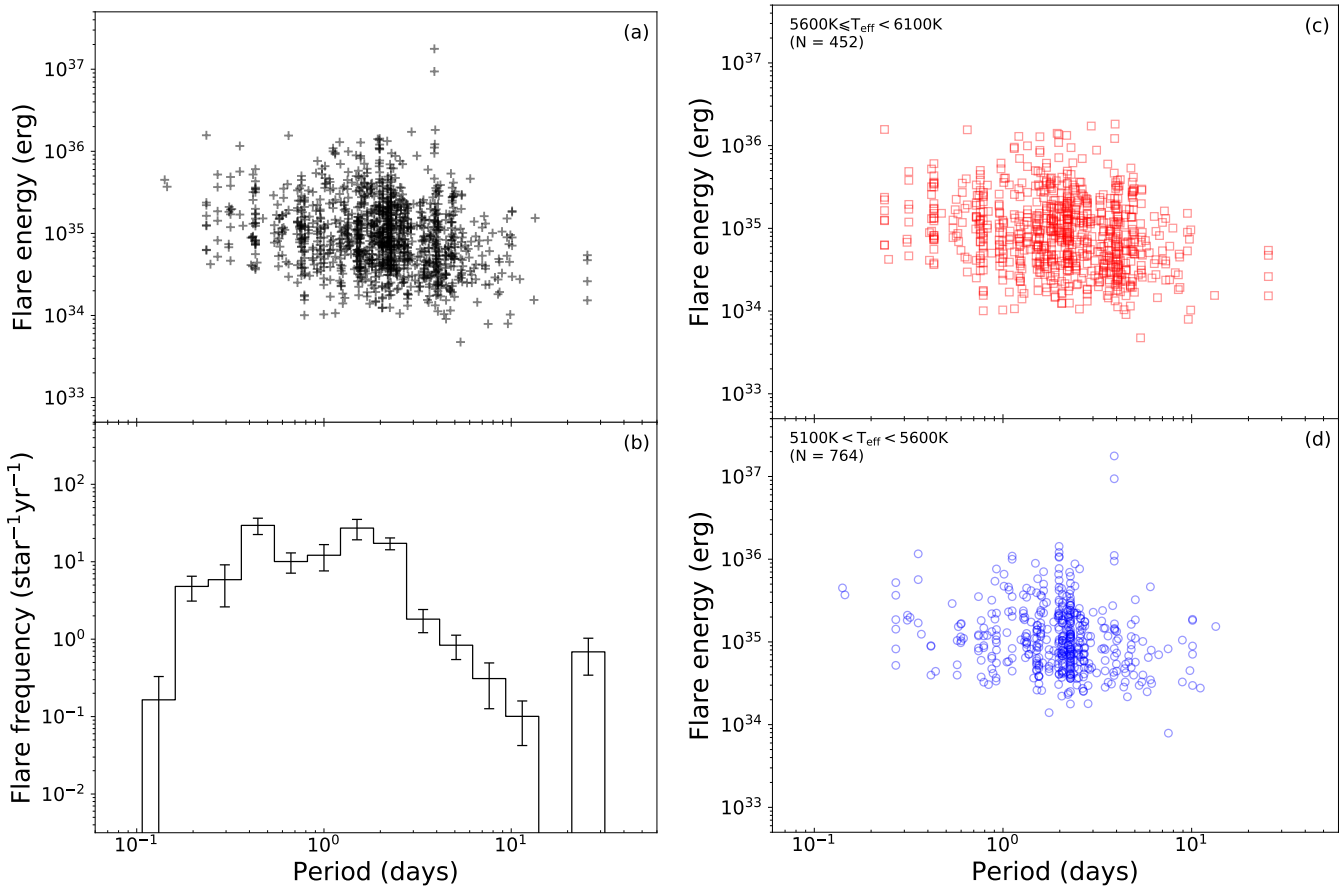

Figure 6. (a) Scatter plot of superflare energy versus stellar period. Black pluses denote every single superflare. (b) Flare frequency of each period bin, the error bars are given by the square root of flare numbers in each bin. (c) and (d) are same as panel (a), but stand for superflares with different effective temperatures 5600K $\leqslant T_{\rm eff} <$ 6000K (red squares)and 5100K $\leqslant T_{\rm eff} <$ 5600K (blue circles), respectively.

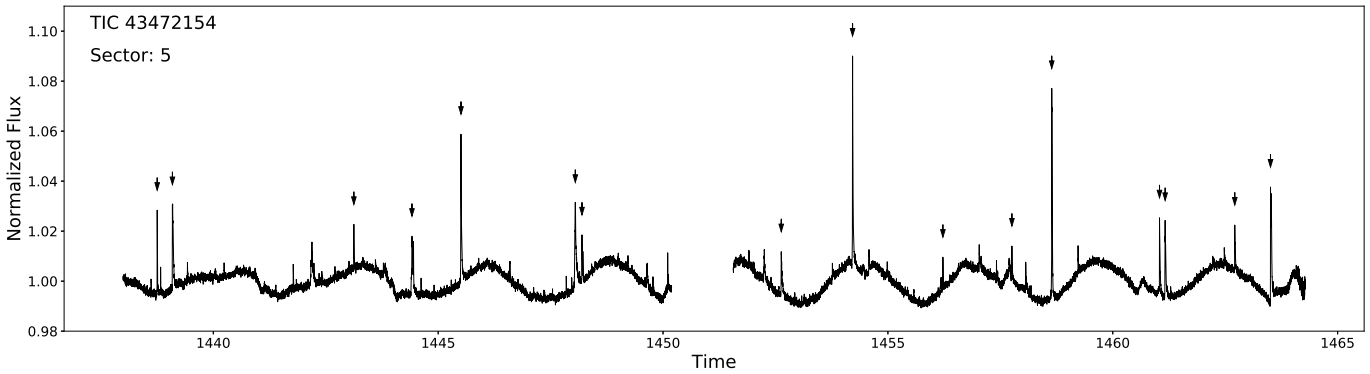

Figure 7. Light curve of TIC43472154. Small arrows are marking those superflares selected from automatic software, and checked through pixel level pattern.

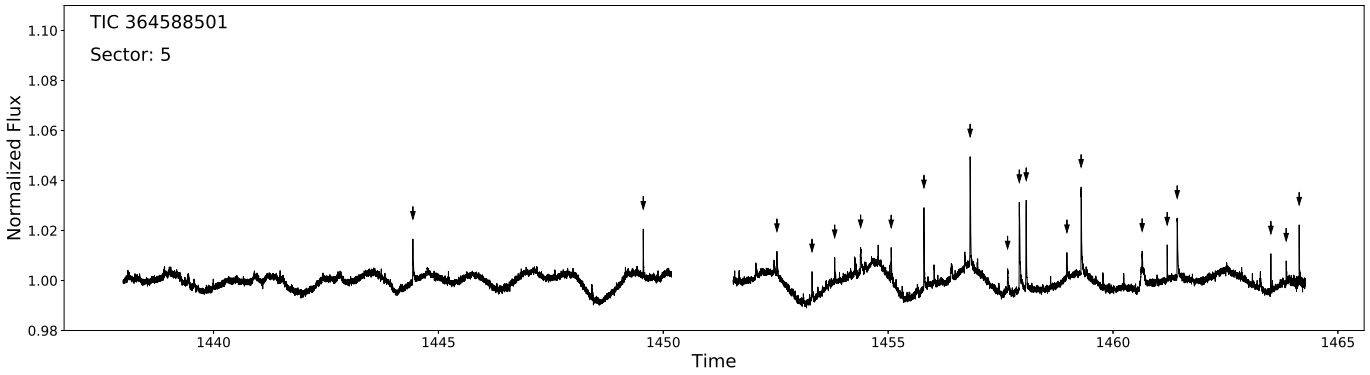

Figure 8. Same as Figure 7, but for TIC364588501.

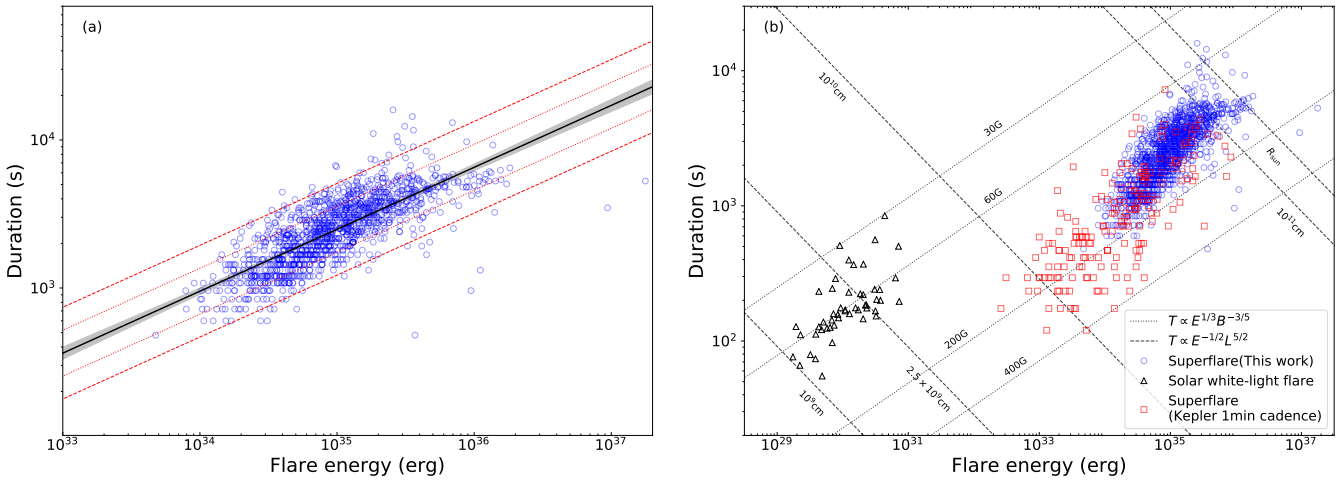

Figure 9. (a) Correlation between superflare energy and duration. The best fitting is marked with black solid line. The gray area represents 95% confidence interval of fitting uncertainties. The red dotted and dashed lines represent 1σ and 2σ interval of extra variability, which is denoted as σ_v in Section 3.1 of Tu & Wang (2018). (b) Comparing superflares in this work (blue circles) with solar white-light flares (black triangles) (Namekata et al. 2017) and superflares found by using short-cadence data of *Kepler* (red squares) (Maehara et al. 2015). The dotted and dashed lines represent scaling laws of Equation (11) and Equation (12), respectively. The coefficients for plotting these lines are the same as Namekata et al. (2017). Here, B represents magnetic field strength, and L denotes flaring length scale.

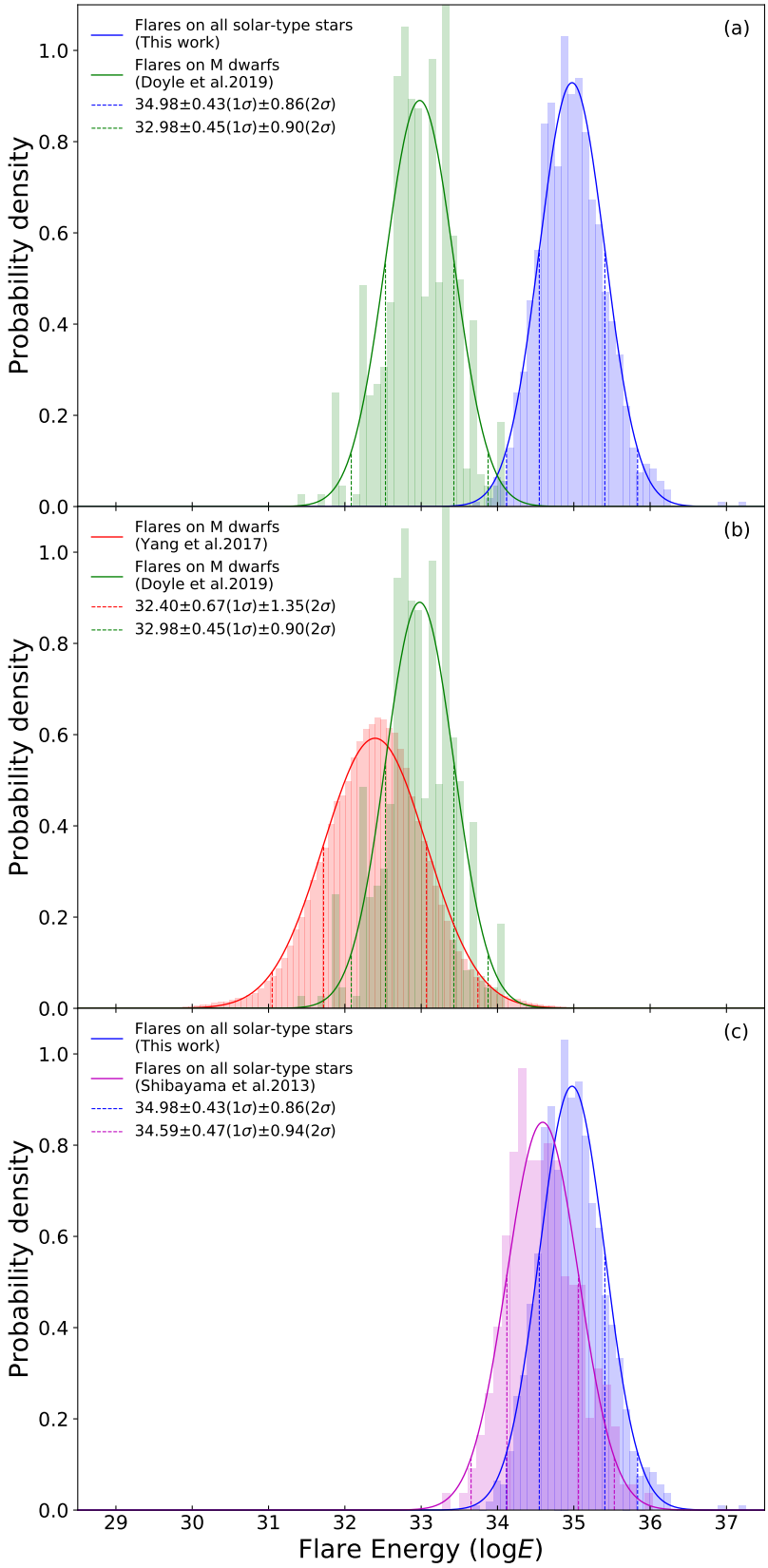

Figure 10. Energy distributions of superflares on solar-type stars (Shibayama et al. 2013, and this work), flares on M dwarfs (Yang et al. 2017; Doyle et al. 2019). In panel (a), the blue histogram shows the results from the superflares on solar-type stars (this work), green stands for flares on M dwarfs (Doyle et al. 2019). These two works both use *TESS* data. In panel (b), flares on M dwarfs are marked as red from *Kepler* data (Yang et al. 2017), and the green histogram is just the same green histogram in panel (a). In panel (c), the magenta histogram represents the superflares on solar-type stars of Shibayama et al. (2013), which used data from *Kepler*. The blue histogram is just as same it in panel (a). The corresponding results of fitting the normal distribution are all listed in the legend of each panel, and shown by the solid colored lines. Dashed lines give standard deviations in ranges of 1σ and 2σ.